Stem Cell Research & Therapy

RESEARCH

Open Access

Tremella polysaccharide microneedles loaded with magnetic dental pulp stem cell intracellular vesicles used for androgenic alopecia

Yonghao Liu[1†], Heng Zhou[1†], Pengcheng Pang[1†], Ye Liu[1], Jieying Situ[1], Junnan Wang[1], Yan He[2*] and Qingsong Ye[1,3*]

Abstract

Background Mesenchymal stem cell exosomes are the most extensively researched type of Extracellular vesicles (EVs) that offer novel avenues for hair regeneration. However, their use in the field of hair regeneration was limited by their poor production of exosomes. It has been discovered that intracellular vesicles (IVs), which are produced at a higher rate than exosomes, play a comparable biological purpose. As a result, we developed HTMI-MN, a microneedle that uses tremella, a type of Tremella polysaccharide (TPS), and hyaluronic acid (HA) as matrix materials. It has magnetic intracellular vesicles (Mag-IVs), which work in concert to treat androgenic alopecia (AGA) and encourage hair growth.

Methods After characterization of the Mag-IVs, we evaluated the effect on angiogenesis by scratch assay, angiogenesis assay, Western Blot and ELISA assay. In addition, we tested the protective effect of Human hair papillary cells (HHDPCs) by CCK-8 method, Western Blot and flow cytometry. Finally, the effects of tremella polysaccharide on M1/M2 polarization of macrophages were detected by fluorescence staining, Western Blot and flow cytometry. AGA model was established in vivo by DHT, and treatment was given by microneedle injection.

Results Our study found that Mag-IVs have greater power to promote angiogenesis and protect HHDPCs from apoptosis compared to other vesicles. Besides, tremella polysaccharide can make the transformation of macrophages to anti-inflammatory phenotype. Taken together, in vivo experiments showed that hair regeneration was faster in HTMI-MN-treated mice.

Conclusion These results indicate that Mag-IVs and tremella polysaccharide can synergistically improve the hair microenvironment, which has a promising future for AGA treatment.

†Yonghao Liu, Heng Zhou and Pengcheng Pang contributed equally to this work.

*Correspondence:
Yan He
helen-1101@hotmail.com
Qingsong Ye
qingsongye@hotmail.com

Full list of author information is available at the end of the article

Keywords Intracellular vesicles, Androgenic alopecia, Dental pulp stem cells lysate, Microneedle, Tremella polysaccharide

Introduction

Androgen alopecia is a common skin disorder that, while not life-threatening, can have an influence on psychological and social activities [1, 2]. According to data, AGA affects 85% of males and 40% of women, and it is more common in young people [3]. high androgen can produce a considerable amount of DHT, which targets and atrophies hair follicles, resulting in the death of microvascular endothelial cells [2–4]. In the early stages of hair loss, vascular degeneration in dermal papilla cells causes an imbalance in the hair follicle ecological niche. Meanwhile, atrophied hair follicles stimulate immune cells and release a vast number of inflammatory factors, exacerbating the hair follicle microenvironment [5, 6].

Exosomes, as a non-cellular therapy that can regulate the biological activity of target cells and overcome the limitations of stem cell transplantation, have been used in the treatment of AGA and other diseases [7, 8]. Although Exo have powerful therapeutic effects, their low production limits their further development. Iron oxide nanoparticles (IONPs) has been reported to stimulate mesenchymal stem cells to express therapeutic growth factors, using exosomes obtained with magnetic nanoparticles and applying static magnetic fields to stimulate mesenchymal stem cells can increase exosome production, and has been shown to have advantages in promoting osteogenesis and angiogenesis, as well as wound healing [9–11]. Dental pulp stem cells (DPSC), as a kind of mesenchymal stem cells originating from neural crest, have the advantages of easy acquisition, easy growth and low immunogenicity. Our previous research found that compared with Exo, IVs extracted from dental pulp stem cell lysates have a higher content, greatly reduce the extraction cost of exosomes. It seems to be more suitable for cell-free treatments in vitro for wound healing which we call Intracellular Vesicles (IVs) [12].

If exosomes are injected directly into the skin, the exosomes are difficult to distribute evenly around the hair follicle, and can also cause some pain [13–15].The microneedle array provides a painless, minimally invasive and controllable transdermal drug delivery system, which has attracted great attention from researchers [16, 17].Specifically, the bioactive ingredient can be encapsulated in the MN needle structure, and the encapsulated ingredient can be released in the dermis by punctured wounds, so that the exosomes can be evenly distributed into the hair follicle microenvironment. However, obtaining better needle tip substrate materials has always been the goal pursued by researchers. Tremella polysaccharide, as a natural polysaccharide material, has excellent biocompatibility and anti-inflammatory properties and has already been applied to some extent. For example, hydrogels using Tremella polysaccharide as a substrate material have shown significant effects in inflammatory diseases such as Crohn's disease and ulcerative colitis. Additionally, it can also improve the mechanical properties of microneedles to a certain extent, making it one of the excellent microneedle substrate materials.

We created a multifunctional HTMI-MN to treat AGA alopecia based on the aforementioned circumstances. These consist of TPS, HA, and Mag-IVs. In order to improve the microenvironment of the hair follicles and break the vicious cycle of AGA hair loss, Mag-IVs were separated, combined with HA@TPS, and encapsulated in the tip of the needle. This allowed the substance to enter the hair loss site, release in the dermis, and control inflammation and angiogenesis while inhibiting the apoptosis of the dermal papilla cells. Furthermore, the patch base may be readily detached after five minutes without leaving any apparent trace. We confirmed in vitro models that the microneedle system can significantly improve the hair follicle microenvironment and promote hair regeneration after 3 doses, providing a potential new approach for the treatment of AGA (Scheme 1).

Materials and methods

Chemicals and materials

Biotay Biotechnology Methanol and tert-butyl hydrogen peroxide (TBHP) from Macklin (Shanghai, China). Polyvinylpyrrolidone (PVP) -K90 and hyperactive hyaluronic acid (Mw < 5 kDa) from Aladdin (Shanghai, China). Polydimethylsiloxane (PDMS) microneedle mold was purchased from Bentengshengwu (Xinxiang, China). Calcein AM, Cell Counting Kit 8 (CCK-8), BCA protein detection Kit, crystal Violet stain, alizarin Red S, Oil Red O, toluidine Blue and dihydroethidium (DHE) were purchased from Biotay Biotechnology (Shanghai, China). Cell staining buffer, mouse TNF-α (tumor necrosis factor α) ELISA kit, mouse IL-10 (Interleukin-10) ELISA kit and human VEGF-a (Vascular endothelial growth factor A) ELISA kit were purchased from Elabscience (Wuhan, China). Radioimmunoprecipitation assay (RIPA) cleavage and mixture purchased from MedChemExpress (USA). Human hair follicle dermal cells (HHDPCs), RAW 264.7 (mouse monocyt-macrophage leukemia cells), and human umbilical vein endothelial cells (HUVECs) were provided by Procell Life Science&Tech (Wuhan, China). Sodium dodecyl sulphate-polyacrylamide gel (SDS-PAGE) and protein marker were purchased from Epizyme Biotech (Shanghai, China). Cell culture plates, matrix

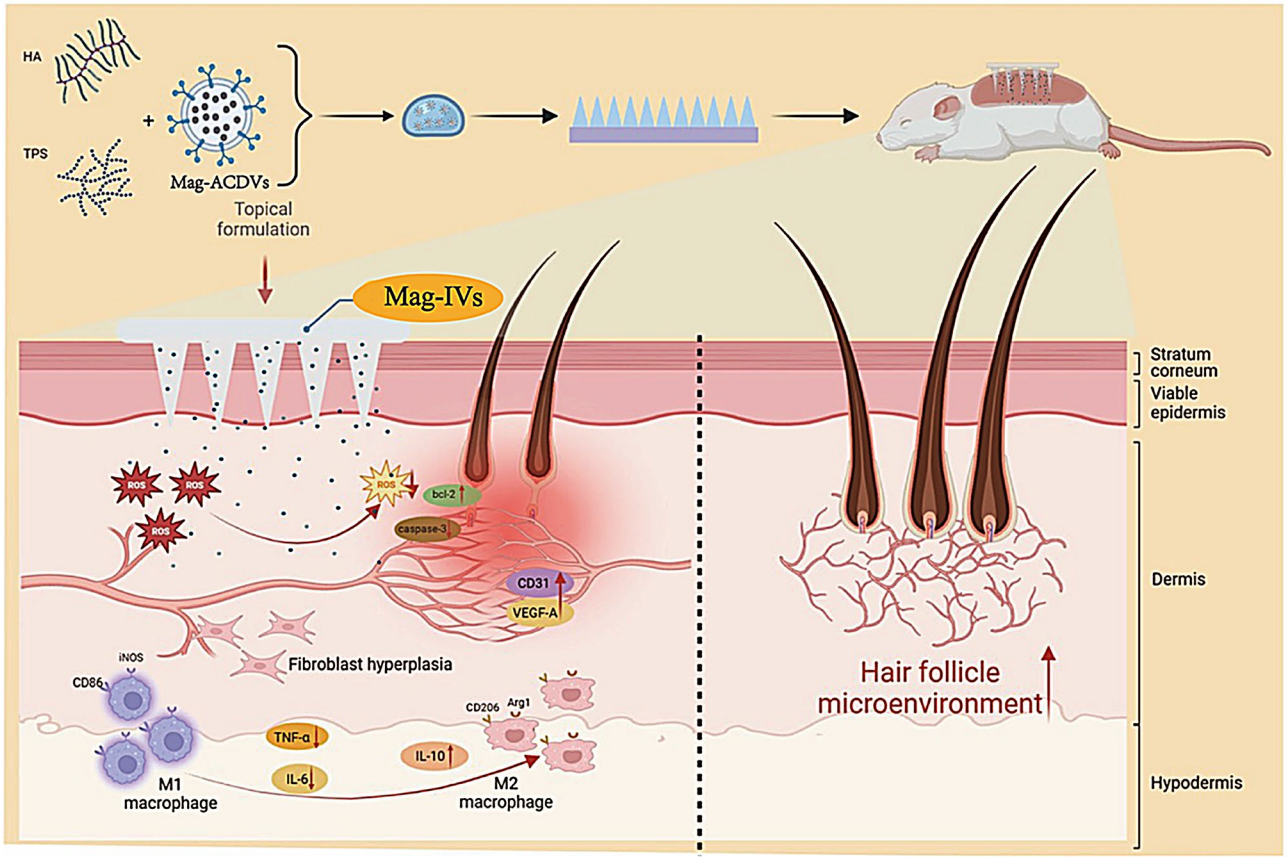

Scheme 1 Schematic illustration of the HTMI-MN for the treatment of androgenic alopecia. Tremella polysaccharide (TPS) and hyaluronic acid (HA) were mixed with Mag-IVs and loaded into the tip of microneedles to form HTMI-MN for the treatment of AGA

glue purchased from Corning (USA). Hematoxylin and eosin (H&E), Rhodamine B (RhB), fluorescein isothiocyanate (FITC), PKH67 Green cell Membrane staining kit, Testosterone and Minoxyl were purchased from Solarbio Science & Technology (Beijing, China). Endothelial cell medium (ECM), collagenase type I and neutral protease were purchased from Sigma-Aldrich. Alpha-modified Eagle Medium (alpha-MEM), Dulbecco Modified Eagle Medium (DMEM), fetal bovine serum (FBS), phosphate buffered saline (PBS) and polyvinylidene fluoride (PVDF) membrane were purchased from Thermo Fisher Technologies (USA). hMSC osteogenic differentiation medium, hMSC lipogenic differentiation medium and hMSC chondrogenic differentiation medium were purchased from Cyagen Biosciences (Suzhou, China). FITC anti-human CD44, FITC anti-human CD45 and FITC anti-human CD73, PE-Cy7 rat anti-mouse CD86, Alexa Fluor 647 rat anti-mouse CD206, fixation/penetration kits were purchased from BD Pharmingen (USA).

Extraction and identification of mesenchymal stem cells

DPSC were used in this study because of their excellent properties and non-ethical constraints. The DPSC was extracted and identified according to our previously established protocol. With the approval of the Ethics Committee of Wuhan University People's Hospital and the informed consent of the donor, the complete third molar of a healthy individual (15–25 years old) was collected from the Department of Stomatology of Wuhan University People's Hospital (Approval Number: WDRY-2022-K025, Wuhan, China). Under sterile conditions, the tooth was dissected and the pulp tissue was separated. The pulp tissue was cut into 1 mm^3 pieces and digested with type I collagenase and protease at 37 °C for 30 min. Cell precipitates were first collected and then suspended in α-MEM containing 20% FBS.

DPSCs are incubated in a standard incubation environment (37 °C, 5% CO2) in α-MEM containing 10%FBS. The medium is changed every 3 days. The DPSC in paragraphs 3 to 5 is used for experiments.

The phenotype and three-line differentiation capacity of DPSCs were determined in accordance with our previously established methods. DPSC was incubated with cell stain buffers containing FITC anti-human CD44, FITC anti-human CD45, and FITC anti-human CD73 antibodies at 4 °C for 30 min. After washing, CytoFLEX flow cytometry (Beckman Coulter, CA, USA) was used to detect the expression of cell surface markers. According

to the manufacturer's instructions, DPSC was induced using hMSC osteogenic differentiation medium, hMSC lipogenic differentiation medium, and hMSC chondrogenic differentiation medium, respectively. Subsequently, the cells were stained with alizarin red S, oil red O and toluidine blue to differentiate into bone, lipid and cartilage, respectively.

Preparation and quantitative analysis of EVs, IVs and Mag-IVs

DPSC was cultured at 37 °C for 2 days using α-MEM containing 10% exotome-free FBS in an environment of 10%O2 and 5%CO2. The supernatant was collected and centrifuged at 12,000 rpm and 4 °C for 30 min to remove impurities and passed through a 200-mesh cell filter. At 90% confluency, DPSCs were harvested using trypsin-EDTA (Gibco, USA) and centrifuged three times in DPBS to remove residual trypsin-EDTA and culture media components.

All DPSC cell vesicles were obtained by ultracentrifugation. Briefly, serum-free cell culture medium was collected and centrifuged at 2000 × *g* for 10 min to remove cellular debris. The supernatants were then collected and centrifuged at 10,000 × *g* for 30 min, and ultracentrifuged twice at 100,000 × *g* for 70 min. The resuspension was sterilized with a 0.22 μm filter disc. EVs was re-suspended with PBS.

To harvest IVs, first cell membrane osmotic rupture was achieved as follows, 1 mL of deionized H2O was added to 1 × 107 cells and incubated for 30 min. Then this cellular suspension was subjected to three freeze-thaw cycles at 80 °C to further dissociate the lysed cell sediments, followed by 30 min of centrifugation at 4000 × g. The supernatants were then purified by two cycles of ultracentrifugation in PBS and the deposited IV was re-suspended in PBS.

To obtain Mag-IVs, we stimulated DPCS with 50 μg/mL IONPs and 100mT static magnetic field for 2 days, and then installed the same method as IV to collect it. After processing the same number of cells, collect EVs, IVs, and mag-IVs, add PBS to a final volume of 1 ml, and perform NTA analysis to compare their yields.Nanoparticle tracking analysis (NTA) was performed using a nanoparticle tracking analyzer (ZetaView, Particle Metrix, GER).

Intracellular uptake of IONPs

Mix thoroughly with FITC at 4 ° C overnight before adding IONPs (NANOEAST, nanjin, China). Then centrifuge 12000r/s for 15 min and wash twice with pbs. DPSC was then inoculated in a 12-well plate and cultured for 24 h, the cells were labeled with lysosomes with Lyso-Tracker (red), nuclei with Hoechst 33,342 (blue), and FITC-labeled IONPs (20 μg/mL, green) were added to the medium. Real-time live cell imaging was captured by inverted inverted fluorescence microscopy (Leica, DMi8, Germany) at 1, 2, 4, and 6 h.

Transmission electron microscope (TEM) analysis

DPSC-EVs, IVs and Mag-IVs are re-suspended in PBS and dripped onto the copper grid. Uranyl acetate DPSC cell vesicles were negatively stained and characterized using transmission electron microscopy (Philips company, Holland Tecnai 12).

Uptake of EVs, IVs and Mag-IVs

According to the manufacturer's instructions, cell vesicles of DPSC were labeled with PKH67 and re-extracted by a fully automated exosome extractor. In order to ensure the complete morphology and function of the in DPSC cell vesicles MN, we inoculated HHDPC in a 12-well petri dish, melted the endosomes containing PKH67 (green) stain with 1mlα-MEM medium, and then absorbed the medium to co-culture with HHDPC. After 6 h, cells were stained with phalloidine (red) for F-actin, and nuclei were stained with DAPI. Images were captured using a fluorescence microscope (BX53, Olympus, Japan).

Scratch assay

HUVEC was inoculated on a 6-well plate, the monolayer was observed by microscope, and the monolayer was marked vertically with 200ul pipette head at uniform speed, and then incubated with PBS, IONPs (20 μg/mL), EVs, IVs, and Mag-IVs (1E + 9Particles/mL). At 0 and 24 h, the cells were washed with PBS and then photographed with an inverted fluorescence microscope (IX71, OLYMPUS, Japan). The intercellular area was measured using ImageJ at 0 h (A1) and 24 (A2) h, and the cell migration rate was calculated as [(A1-A2) /A1]×100%.

Matrigel assay

Matrix glue solution is prepared by combining matrix glue with PBS in a ratio of 1:1 on ice. The matrix glue solution was then added to the 96-well plate (100μL per well) and placed at 37 °C for at least 1 h. HUVEC (5 × 104 cells per well) was inoculated in a matrix gel-coated plate and incubated with ECM containing PBS, IONPs(50 μg/mL), EVs, IVs, and Mag-IVs (1E + 9Particles/mL) for 6 h. The tubular structures were observed using an inverted fluorescence microscope (IX71, OLYMPUS, Japan) and analyzed by ImageJ (Angiogenesis).

Western blot

The cells are treated accordingly. The protein was extracted with RIPA cracking buffer supplemented with the mixture, and the concentration was determined by BCA method. After boiling the sample buffer, the protein samples were isolated by SDS-PAGE electrophoresis and transferred to PVDF membrane. Subsequently,

PVDF membrane was sealed with 5% skim milk and incubated with primary antibody at 4 °C for 15 h, including anti-CD206(Proteintech,60143-1-Ig,1:2000), anti-SOX9(Proteintech,67439-1-Ig,1:2000),anti-iNOS(Proteintech,18985-1-AP,1:2000), anti-TSG101 (Proteintech, 67381-1-Ig, 1: 1000), anti-HSP70 (Proteintech, 66183-1-Ig, 1:1000), anti-ALIx (Proteintech, 67715-1-Ig, 1: 1000), anti-CD63 (Proteintech, 67605-1-Ig, 1:1000), anti-BCL2 (Proteintech, 68103-1-Ig, 1: 2000), anti-BAX (Proteintech, 60267-1-Ig, 1:2000), anti-C-Cas3 (abcam, ab2302, 1:500), anti-C-Cas9 (CST, 9505, 1: 5000), anti-VEGF-A (abcam, ab46154, 1:500), anti-IL-1 Beta (Proteintech, 66737-1-Ig, 1:2000), anti-ARG1 (abcam, ab239731, 1: 5000), anti-IL10 (CST, 12163, 1:500), anti-CD86 (Proteintech, 13395-1-AP, 1:2000), anti-beta-actin (Servicebio, GB15001, 1: Primary antibody 1000, China), GAPDH (Servicebio, GB15002-100, 1:1000, China). The next day, the membrane was incubated with the corresponding secondary antibody and scanned using a gel imaging system (ChemiDoc, BIO-RAD, USA).

Enzyme linked immunosorbent assay (ELISA)

HUVEC and RAW264.7 cells were treated as described above. After 24 h, the supernatant was collected and VEGF, TNF-α and IL-10 ELISA were performed according to the manufacturer's instructions.

Flow cytometry

RAW264.7 cells were induced M1 polarization by LPS (1 μg/mL) and incubated with TPS (0, 20 and 50 μg/mL) for 24 h. Digest the cells and prepare a single-cell suspension. The cells were blocked with Fc blocks and then stained at 4 °C for 30 min with PE-Cy7 rat anti-mouse CD86 antibody (560582) and PE-Cy7 rat IgG2a, κisotype control (552784). After fixation and permeation, cells were stained at 4 °C for 30 min with Alexa Fluor 647 rat anti-mouse CD206 antibody (565250) and Alexa Fluor 647 rat IgG2a, κisotype control (557690). The cells were analyzed using flow cytometry (CytoFlex, Beckman Coulter, USA).

CCK-8 detection and crystal violet staining

To determine the optimal range of IONPs and static magnetic field, DPSC (5 × 103 cells/well) was inoculated in 96-well plates and incubated with IONPs (0, 25, 50, 100, 150 μg/mL) for 1, 2, and 3 days.

Synergistic protective effect of endosomes on DHT-damaged HHDPCs DHT was used to induce cell damage models, similar to previous studies [5]. In brief, HHDPCs (1 × 103 cells per well) were inoculated on a 96-well culture plate. After 24 h, D-MEM solution containing DHT (5 nmol/mL), PBS, IONPs(50 μg/mL), EVs, IVs, and Mag-IVs (1E + 9Particles/mL) was used to replace the cell medium. 48 h. Normal cell culture medium was used as control. Cell survival rates in different groups were measured as described above. At the same time, the cells were fixed with 4% paraformaldehyde solution and stained with crystal violet (CV) for 1 min, and optical images were obtained using the above optical microscope.

Preparation and characterization of MN

In this study, polydimethylsiloxane (PDMS) micromolds consisted of 15 × 15 tetrahedral needle cavities, each with a base surface size of 360 μm and a height of 800 μm. For HA-MN, 50 μL of freshly prepared HA solution (500 mg/mL) was carefully added to the micromold and allowed to flow slowly to cover all needle cavities. The micromold was centrifuged (3,000 rpm, 10 min) and vacuumed to ensure that the solution completely filled the needle cavity. Gently remove excess solution and dry the mold at 37 °C for 2 h. Subsequently, 200 μL PVP-K90 solution (20%) was dropped onto the mold and allowed to flow slowly. After incubation at 37 °C overnight, HA-MN was obtained. In addition, HT-MN is a microneedle made from a matrix material consisting of a solution of HA (500 mg/mL) and TPS (150 mg/mL), while HTE-MN, HTI-MN, and HTMI-MN are obtained by adding 1E + 5 particles/mL of EVs, IVs, and Mag-IVs to the HA and TPS mixed solution. Rhb-mn was prepared by adding RhB (0.1%, w/v) to the HA solution.

The optical morphology of MN was photographed with a microscopic imaging device (SZ51, OLYMPUS, USA). SEM images of MN were taken using field emission scanning electron microscope scanning (CLARA, TESCAN, CZ).

Distribution of DPSC-EVs, IVs and Mag-IVs in MN

As shown by the above cell vesicle staining method, the PKH67-labeled cell vesicles were obtained and mixed with HA and RhB to produce evs-RhB-MN in the same way. Fluorescence images of MN were observed using a fluorescence microscope (BX53, Olympus, Japan).

Mechanical properties and slow-release ability of MN

The mechanical strength of MN was tested using an electronic universal testing machine (CMT6103, MTS, USA). MN is fixed on a flat surface with the tip facing up. The loading rate is set to 0.3 mm/min and the displacement is set to 800 μm.

RhB-MN was placed in a cell culture dish and immersed in PBS. The dissolution process was recorded using a fluorescence microscope (BX53, OLYMPUS, Japan).

According to the previous method, microneedles were immersed in 1mlpbs upside down, and appropriate solution was absorbed at 10, 30, 60, 120, and 300s, and the protein concentration was determined by BCA [5].

Animal and moral statement

Forty-two male KM mice (7 weeks old) were purchased from the Experimental Animal Center of China Three Gorges University (Yichang, Hubei, China) and fed for one week. All surgical procedures were approved by the Experimental Animal Ethics Committee of the People's Hospital of China Affiliated to Wuhan University (20231003 C). The work has been reported in line with the ARRIVE guidelines 2.0.

Surgery and treatment

To establish the AGA model, the back skin of 8-week-old mice was shaved and a testosterone solution (0.2%, w/v) was applied to the hair removal area daily for 14 days. Due to the short action time of microneedles, isoflurane inhalation anesthesia was used (Laboratory of Animal Center, Wuhan University People's Hospital). The mice were randomly divided into 7 groups (based on the literature, 6 mice per group is reasonable): (1) AGA, (2) HA-MN, (3) HT-MN, (4) THE-Mn, (5) HTI-MN, (6) HTMI-MN (7) Minoxidil. Since HA has been widely used as a matrix material in microneedle systems, we established the HA-MN group as a control to demonstrate the role of TPS. Additionally, we selected Minoxidil, a common treatment for androgenetic alopecia, as a positive control to highlight the excellent potential of the microneedle system in hair regeneration. The AGA model mice without any treatment served as the control group. Mice in the experimental group received the corresponding MN patch on days 3, 8 and 12 after shaving. These MN patches were inserted into the dorsal skin using a microneedle syringe and pressed for 1 min, then the backing layer was removed after 5 min. Minoxidil was applied topically daily to the back of AGA mice as a positive control group. For each mouse, try to ensure that the basic conditions such as sunlight temperature are consistent to exclude the influence of confounding factors. Take digital photos of the back area and measure hair density with the help of a skin microscope. Since the AGA model mice had little effect on the health status of each mouse, all mice were included in the evaluation. After 14 days, the mice were killed using carbon dioxide inhalation, and skin tissue was taken for further testing.

The experimenter was not the designer of the experiment to exclude the influence of subjective factors on the experimental results.

In vivo imaging study

DiR-labeled IVs, administered through direct injection or encapsulated in HA-MN and HT-MN, were applied to the mouse skin. Imaging was performed on each mouse using the IVIS Spectrum imaging system (PerkinElmer EnSight, USA) at 30 min, 12 h, 1 day, 2 days, and 3 days post-treatment.

Scanning electron microscope (SEM) analysis

Hair samples were collected from all groups of mice on day 14 after shaving. Subsequently, the sample was gold-plated and observed using a field emission scanning electron microscope (Tescan MIRA, Tescan, Czech Republic). The diameter of root hair shaft was measured and analyzed.

Hematoxylin and eosin (H&E) stains

On the 14th day after shaving, the mice were euthanized. Skin samples from the shaved area were fixed, embedded and prepared into paraffin sections. Sections were stained with H&E staining kit and observed under a bright field microscope (BX53, OLYMPUS, Japan). Hearts, livers, spleens, lungs and kidneys of mice were collected and stained for biocompatibility.

Immunohistochemical stains

The sections were closed with 1% bovine serum albumin (BSA) at room temperature (RT) for 1 h. These slices were incubated with anti-cytokeratin-19 primary antibody (abcam, ab133496) and then incubated with rabbit secondary antibody and stained with DAPI. Images were captured under a bright field microscope (BX53, OLYMPUS, Japan) and analyzed using ImageJ.

Immunofluorescent stains

After antigen repair, the section was closed with 1% BSA for 30 min. These slices were incubated with anti-KI67 (abcam, ab279653), anti-SOX9 (abcam, ab185966) and anti-CD31 (proteintech, 11265-1-AP) primary antibodies. They were then incubated with the corresponding FITC-labeled goat anti-mouse, CY3-labeled goat anti-rabbit, and FITC-labeled goat anti-rabbit secondary antibodies and stained with DAPI. Images were obtained using a fluorescence microscope (BX53, Olympus, Japan) and analyzed using ImageJ.

DHE staining

On the 14th day after shaving, skin samples from the hair removal area were prepared as frozen slices. The frozen slices were incubated with DHE (2.5μM) for 30 min and re-stained with DAPI. Images were collected using a fluorescence microscope (BX53, Olympus, Japan) and analyzed using ImageJ.

Statistic analysis

To verify the consistency of the data, all experiments were repeated three times. Data analyzed using GraphPad Prism (version 9.0) are represented as mean ± standard deviation (mean ± SD). The experimental data were statistically analyzed by one-way analysis of variance. ns, no significant ($p > 0.05$), $^{*}p < 0.05$, $^{**}p < 0.01$, $^{***}p < 0.001$, $^{****}p < 0.0001$.

Result

Acquisition, identification and uptake of Mag-IVs

First of all, DPSC were identified by reference to previous methods (Fig. S1). Then in order to prove that IONPs can be taken up by DPSC, we referred to the previous methods [18]. Immunofluorescence showed that IONPs(green) and lysosomes(red) had a lot of co-locations (Fig. 1A), and the fluorescence intensity increases with time (Fig. 1B), indicating that IONPs entered cells through endocytosis and accumulating in lysosomes. Then, in order to screen suitable IONPs concentration and static magnetic field intensity, we co-cultured IONPs with DPSC at different concentrations (0, 25, 50, 100, 100 μg/mL). CCK-8 results showed that DPSC had better value-added ability under 50 μg/mL IONPs treatment. This is similar to the results of previous studies [19, 20]. Similarly, IONPs were cultured with an optimal concentration of 50 μg/mL and given a series of concentration gradients of static magnetic fields. Finally, CCK-8 results showed that IONPs at 50 μg/mL and static magnetic field intensity at 100mT were the most suitable for DPSC proliferation, which was consistent with the results of previous studies (Fig. 1D and E). Furthermore, because ROS attacks AGA-damaged hair follicles, and because IONPs have been shown to have some anti-ROS activity, we looked at IONPs' in vitro anti-ROS ability in DPSC. When DPSC was stimulated by 100 μmol/ml TBHP, IONPs shown some ROS resistance. (Fig. 1C).

We then quantified and characterized sources from DPSC-EVs, IV, and Mag-IVs. TEM showed that these EVs were mostly spherical and semi-arcuate, with sizes ranging from 50 to 150 nm (Fig. 1F). We determined the volume of EVs extracted from the same amount of cells to 1 ml, and then conducted NTA analysis. The result shows that the particle concentration of Mag-IVs is 6.8E + 11Particles/mL, which is significantly higher than that of IVs (1E + 11Particles/mL) and DPSC-EVs (3.4E + 10Particles/mL). However, there is no significant difference in particle size (Figure. S2). In order to confirm the stronger therapeutic effect of Mag-IVs, vesicae of the same particle concentration are used in subsequent treatments. According to relevant literature, DPSC cell vesicles is 1E + 9Particles/mL in in vitro cell experiments, and 1E + 5 Particles/g is used for microneedle injection in animal models. Finally, we used Western blot to verify these EVs markers, Western blotting revealed that these EVs expressed TSG101, CD63, HSP70, and ALIX, but not calnexin (Fig. 1H).

In order to check whether HHDPC can take up DPSC cell vesicles and whether there is a difference in uptake capacity, we Mark DPSC cell vesicles with PKH67 according to the reagent manufacturer's method, and then co-cultured DPSC cell vesicles with HHDPC with the same particle number for 12 h. We then stained the cytoskeleton with ghost-ring peptides and measured the DPSC cell vesicles uptake rate by HHDPC using inverted fluorescence microscopy. As shown in Fig. 1F and G, the uptake of Mag-IVs was significantly higher than that of IVs ($P < 0.05$) and DPSC-EVs($P < 0.001$), and there was a significant statistical difference. In summary, our results suggest that Mag-IVs has the advantage of higher yield and easier uptake by HHDPC compared with the other two groups.

DPSC cell vesicles' activation impact on HUVEC

In addition to protecting hair follicle stem cells directly, activating undamaged endothelial cells to migrate to the hair loss area and improving the microenvironment in the hair loss area are also essential for hair regeneration. There is a lot of evidence that MSCs have the ability to improve angiogenesis by producing large amounts of growth factors through paracrine action [21].Therefore, we studied the activation effect of Cell vesicles of DPSC on HUVEC. First, we compared the migration ability of HUVEC under different treatments by in vitro scratch experiments (Fig. 2A). In addition, since Mag-EVs obtained after INOPs treatment have been reported to encapsulate a certain amount of INOPs, in order to eliminate this part of interference, we used INOPs to treat HUVEC. The results showed that Mag-IVs group showed the best migration promoting activity. Quantitative analysis further proved that the Mag-IVs group had the best migration promoting ability, and IV was the second highest, which was more advantageous than DPSC-EVs (Fig. 2F). We then evaluated the effect of Cell vesicles of DPSC on angiogenesis. As a result, HUVECs treated with Mag-IVs formed more branched tubular structures (Fig. 2A). Quantitative measurements showed that Mag-IVs significantly promoted the formation of vascular structure structures, characterized by more junctions, compared to the control group and the DPSC-EVs group (Fig. 2C). Studies have shown that VEGF plays a leading role in regulating angiogenesis and vascular permeability by guiding cell proliferation, migration, and survival. Next, Western blot analysis and Elisa were used to further compare VEGF content in different treatment groups. Quantitative analysis showed that the intracellular protein content of VEGF and the cytokine content in the supernatant in the Mag-IVs group were the highest (Fig. 2B, D and E). These results suggest that among all cell vesicles of DPSC, the Mag-IVs group is more effective in promoting angiogenesis, which may be related to the higher particle concentration and its higher presence of related growth factors, ultimately leading to greater expression of VEGF.

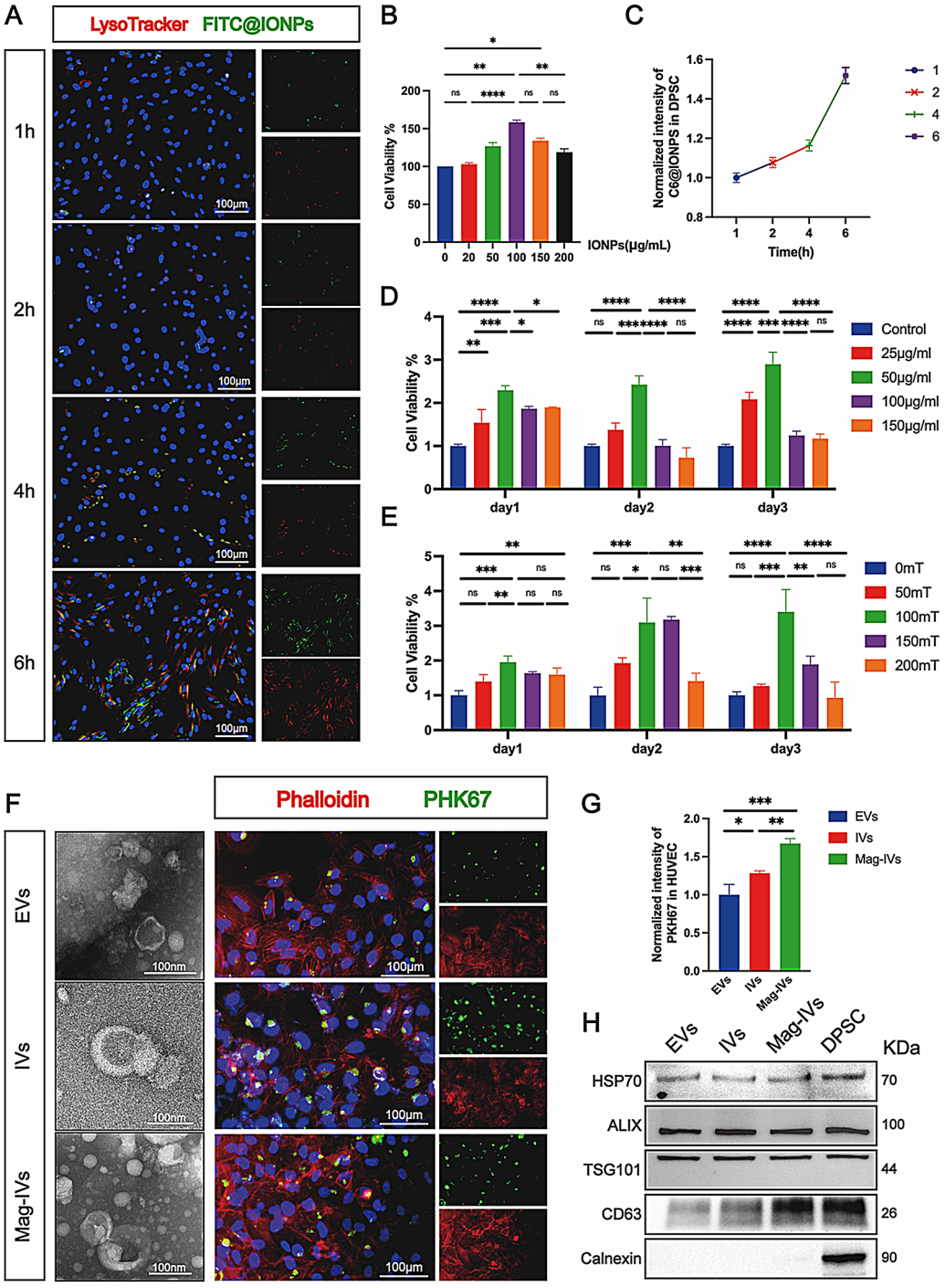

Fig. 1 Preparation, uptake and identification of Cell vesicles of DPSC (**A**) FITC-labeled IONPs in DPSCs (50 μg /ml; Green fluorescence) intracellular transport. LysoTracker (red) is used to label the lysosome and Hoechst 33,342 (blue) is used to label the nucleus. (**B**) cck-8 results of IONPs treated with different concentrations under TBHP stimulation of 100 μmol/ml. (**C**) Changes in the relative fluorescence intensity of FITC-labeled IONPs. (**D**) The proliferation of DPSCs cultured in IONPs nanoparticles at different concentrations was measured by CCK-8 assay. (**E**) Proliferation of DPSCs treated with IONPs nanoparticles at an optimal working concentration (50 μg/mL) and exposed to varying SMF intensities. (**F**) TEM analysis of Cell vesicles of DPSC PHK67 (green fluorescent) labeled EVs are taken up by HHPDC, ghost pen cyclic peptides are used to label the cytoskeleton (red fluorescent), and Hoechst 33,342 (blue) is used to label the nucleus. (**G**) Fluorescence intensity statistics at 12 h. (**H**) Protein imprinting analysis of Extracellular vesicles proteins TSG101, CD63, HSP70, ALIX and Calnexin. ns, nonsignificant ($p > 0.05$), $*p < 0.05$, $**p < 0.01$, $***p < 0.001$, $****p < 0.0001$

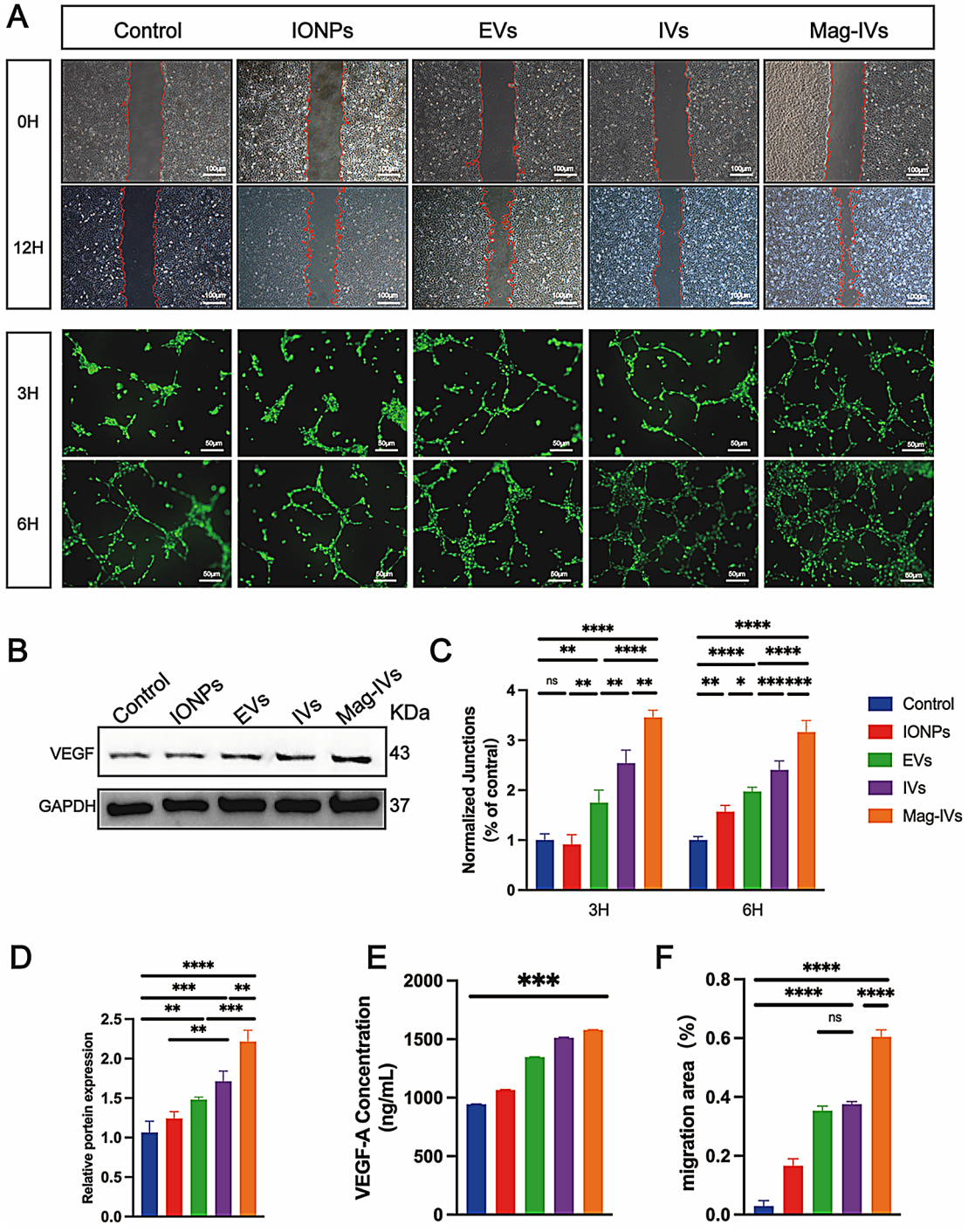

Fig. 2 The ability of DPSC-EVs to promote angiogenesis in vitro. (**A**) Scratch experiments were conducted to compare the mobility effects of HUVEC 0–12 h in different treatment groups. Representative microscopic images of HUVEC tube formation at 3 h and 6 h under different treatments. (**B**) Western blot analysis of VEGF after 12 h culture. (**C**) Quantitative analysis of tube formation assay ($n = 3$, mean ± SD) (**D**) Quantitative analysis of western blot assay ($n = 3$, mean ± SD). (**E**) Quantitative analysis of VEGF in HUVEC supernatant after 12 h culture $n = 3$, mean ± SD. (**F**) Cell mobility analysis of HUVEC after 12 h culture $n = 3$, mean ± SD. ns, nonsignificant ($p > 0.05$), $*p < 0.05$, $**p < 0.01$, $***p < 0.001$, $****p < 0.0001$

TPS regulated M1/M2 macrophage polarization

The inflammatory environment around hair follicles is also one of the important factors affecting hair growth, so we studied the ability of TPS to regulate the polarization of macrophages (Fig. 3A). First, LPS treated macrophages showed M1 phenotype (iNOS high expression), and TPS inhibited M1-like polarization and promoted its transformation to M2 phenotype (Arg1 high expression),

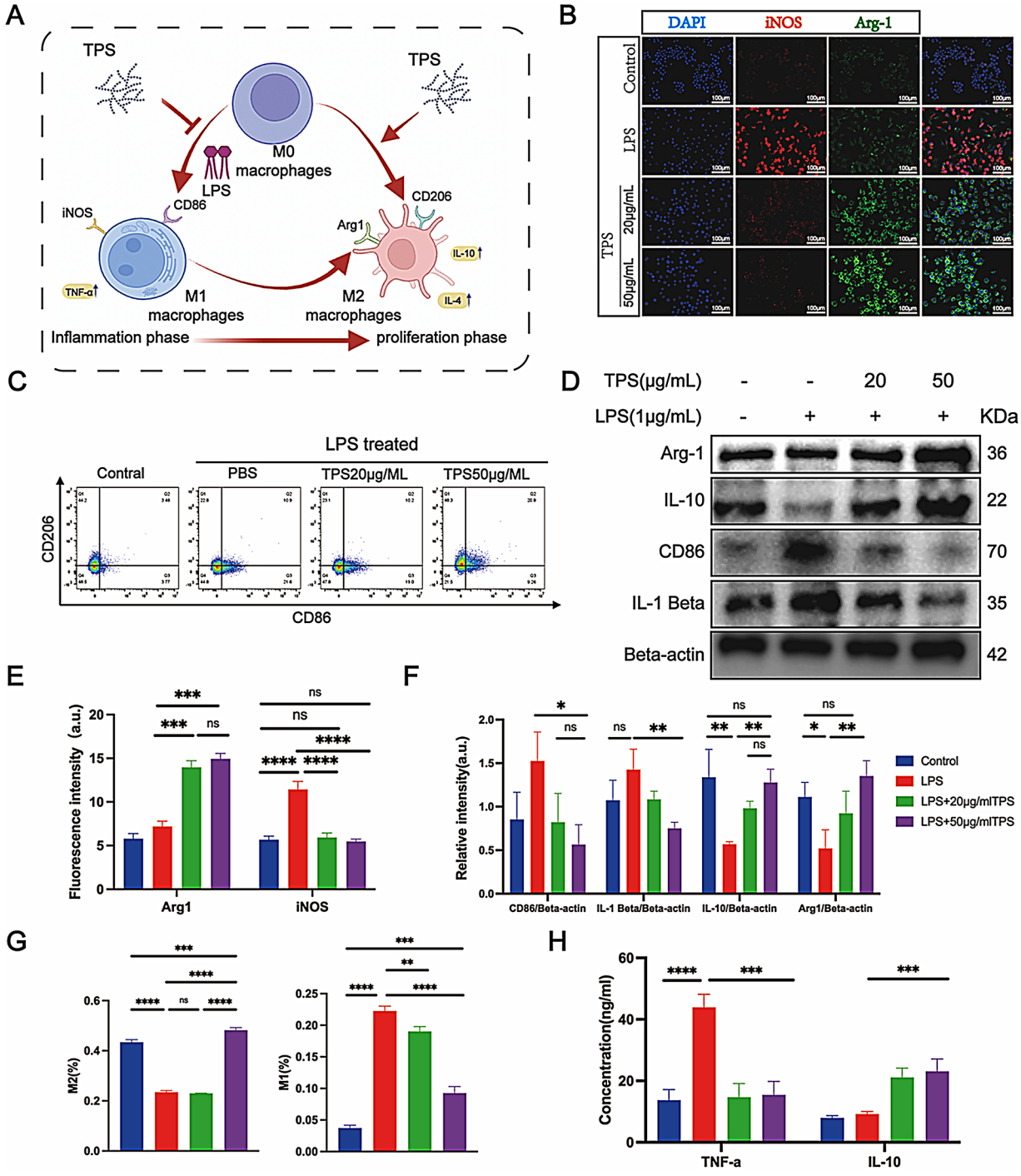

Fig. 3 Macrophage phenotype regulation based on TPS. (**A**) Schematic diagram of TPS regulating macrophage polarization. (**B**) Representative immunofluorescence images of RAW264.7 cultured under LPS and treated with TPS, M1 macrophages labeled with (iNOS: red fluorescence), M2 macrophages labeled with (Arg1: green fluorescence) and (DAPI: blue fluorescence.) (**C**) the Flow cell analysis results of RAW264.7 (at F4/80 + and CD11b + gated) treated with different concentrations of TPS under LPS. (**D**) Western Blot analysis of CD86,Arg1,IL-10,IL-1 Beta treated with LPS and different concentrations of TPS. (**E**) Quantitative results of immunofluorescence. (**F**) Quantitative results of protein immunoblotting. (**G**) Quantitative results of Fluidic cell surgery. (**H**) Changes in inflammatory cytokines TNF-α and IL-10 after TPS treatment. culture $n = 3$, mean ± SD. ns, nonsignificant ($p > 0.05$), $*p < 0.05$, $**p < 0.01$, $***p < 0.001$, $****p < 0.0001$

and the regulatory effect of TPS50 μg /ml was stronger than that of 20 μg /ml, indicating a certain concentration dependence (Fig. 3B and E). Similarly, the Flow cell analysis showed similar results, with the polarizability of F4/80 + and CD11b + macrophages reaching 21.6% after 24 h LPS induction, while that of M1 macrophages significantly decreased after TPS treatment (Fig. 3C and G). Western blot showed that CD86 levels in LPS treated group were higher than those in control group. This suggests that LPS-induced macrophages are in an inflammatory state. When TPS was used, the level of CD86 was significantly reduced. Compared with the control group, LPS group significantly expressed Inflammation-related protein IL-1 Beta and lower expression anti-inflammatory related proteins of iL-10 and Arg1, which were inhibited by TPS and showed a concentration dependence similar to the previous results (Fig. 3D and F). Further, we detected the inflammatory cytokines of macrophages treated with TPS, and compared with the two groups treated with TPS, the pro-inflammatory factor TNF-α was decreased in LPS group and the anti-inflammatory factor IL-10 was slightly increased (Fig. 3H). Together, these results suggest that TPS can inhibit the polarization of M1 macrophages, promote the secretion of anti-inflammatory cytokines by immune cells, and regulate the inflammatory microenvironment around hair follicles.

DPSC cell vesicles' synergistic protective action on HHDPCs with DHT damage

We used dihydrotestosterone (DHT,5nmol/ml) to establish an HHDPCs model of injury. As shown in Fig. 4A, crystal violet staining of HHDPCs confirmed the successful establishment of the cell damage model, because DHT treatment significantly reduced the proliferation of HHDPCs, and there were certain changes in cell morphology, while the use of IONPs and DPSC cell vesicles significantly reduced DHT-induced cell damage and the proliferation of HHDPCs was promoted. The CCK-8 experiment further quantitatively demonstrated the protective effect of DPSC cell vesicles AGAinst HHDPCs, and the effect of Mag-IVs was more obvious than that of the other two groups as time increased (Fig. 4B). Antioxidant and apoptotic abilities are very important for HHDPCs to survive DHT damage. In order to study the antioxidant and apoptotic effects of DPSC cell vesicles on HHDPCs, we constructed a damage model of HHDPCs using DHT, and then used ROS fluorescence kit to detect the ROS content of cells. As shown in Fig. 4C, DHT significantly increased ROS content, while DPSC cell vesicles showed its ability to clear ROS. Fluorescence quantitative analysis showed that there were obvious differences between the Mag-IVs group and other groups, showing excellent ROS resistance, which may be related to the synergistic effect of Mag-IVs of IONPs (Fig. 4D). Then, we used flow cytometry to detect apoptosis induced by different treatment groups (Fig. S2 B). Similar to the previous results, Mag-IVs significantly reduced the apoptosis of HHDPCs. Western blot further confirmed its effect on HHDPCs apoptosis reversal. DHT significantly inhibited the expression of anti-apoptotic protein Bcl-2 in HHDPCs, and promoted the expression of apoptotic proteins Bax, cleaved-caspase3 and cleaved-caspase9. After Mag-IVs treatment, the expression levels of BAX, cleaved-caspase3, cleaved-caspase9 and Bcl-2 recovered (Fig. 4E and F), and quantitative analysis showed significant differences. In conclusion, these results suggest that DPSC cell vesicles can help HHDPCs resist DHT-induced apoptosis and oxidative stress damage.

Preparation and characterization of separable microneedles

Separable microneedles can be prepared based on the solubility difference between PVP matrix and HA-TPS (Fig. 5A). First, Fourier characterization of TPS is carried out (Fig. S2C). Then we used different concentrations of HA and TPS to synthesize soluble tip. Together with earlier research [22, 23], 500 mg/mL HA was chosen as the matrix material in order to provide an appropriate tip structure. TPS of varying contents was then blended to create a number of mixed solutions with concentration gradients. The solution would become overly viscous and make it challenging to create microneedles if an excessively high concentration of TPS was added. Consequently, TPS at concentrations of 10, 50, 75, 150, and 300 mg/mL was ultimately chosen, and the resulting microneedles' force displacement curve was examined. The findings demonstrated that the microneedles will become more fragile and fracture at a pressure of 100 N if the TPS concentration is too high (300 mg/mL) or too low (10 mg/mL or 50 mg/mL). Both 75 mg/mL and 150 mg/mL TPS microneedles have comparable mechanical characteristics and can tolerate 200 Newtons of pressure(Fig. S4). The optimal selection for the microneedle tip material was 500 mg/mL HA plus 150 mg/mL TPS in order to boost the dose of TPS in vivo. The base surface size of each needle is 360 μm, the height is 800 μm, and the overall shape is pyramidal (Fig. 5B).

We then photographed the PKH67 (green fluorescence) labeled IVs and Rhodamine B (red fluorescence) labeled HA-TPS matrix under a fluorescence microscope, and the fluorescence images proved that DPSC cell vesicles were evenly distributed at the tip of the needle (Fig. 5C). The forced-displacement curve proves that the microneedles have a high enough mechanical strength (Fig. 5D) to be easily inserted into the skin. Finally, we evaluated the slow-release ability of microneedles. As shown in Fig. 5E,

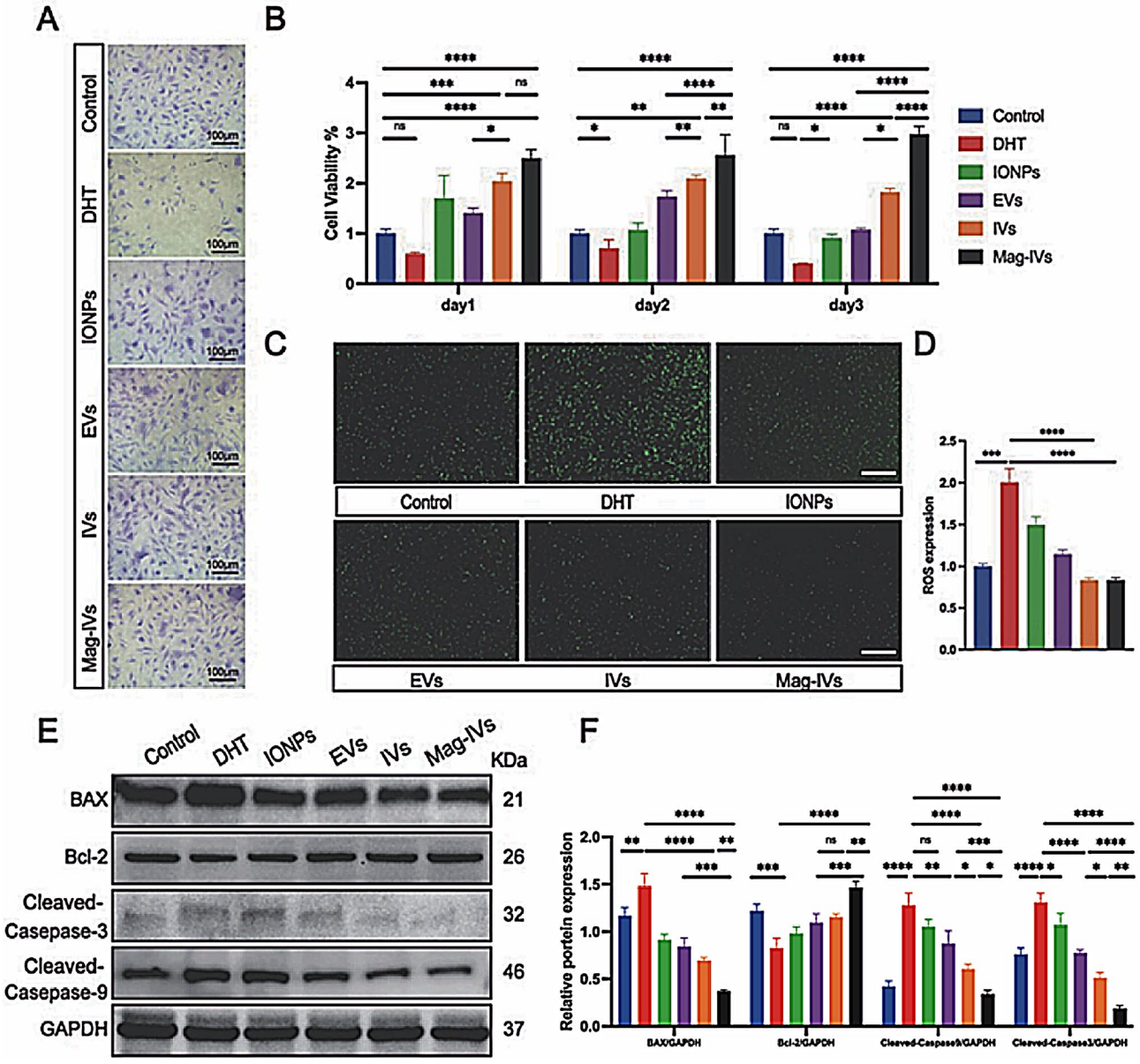

Fig. 4 DPSC cell vesicles protects human hair follicle dermal papillary cells (HHDPCs) from DHT damage. (**A**) Representative images of crystal violet staining after different treatments. (**B**) Proliferation and viability of DHT-damaged HHDPCs under different treatments (1, 2, 3 days) ($n = 3$) (**C**) ROS fluorescence staining (Scale bar: 100 μm) and (**D**) fluorescence quantitative analysis. (**E**) HHDPCs are treated with DHT and DPSC-EVs combined. Western Blot was used to detect Bcl2, BAX, cleaved-Caspase-3, cleaved-Caspase-9 and GAPDH, and (**F**) quantitative statistics were performed for gray values. culture $n = 3$, mean ± SD. ns, nonsignificant ($p > 0.05$), $*p < 0.05$, $**p < 0.01$, $***p < 0.001$,$****p < 0.0001$

microneedles almost completely dissolved in 60s under the condition of simulating body fluid humidity, and quantitative analysis also proved that microneedles completely released DPSC cell vesicles around 60s (Fig. 5F).

HTMI-MN is used in the treatment of hair regeneration in mice

To verify the efficacy of hair regeneration in vivo, we applied DHT (2%) to C57BL/6 mice continuously for 7 days after shaving to form an AGA model. It is then treated by inserting a microneedle or topical application with 3% minoxidil. As shown in Fig. 6D, different MN was applied to the depilatory area of mice on days 3, 8, and 12, or minoxidil was given, and photographs were taken on days 7, 10, and 14. As shown in Fig. 6B, the in vivo imaging photos reveal the distribution of IVs during the 7-day treatment. The microneedles completely dissolve 5 min after piercing the skin, and significant fluorescence appears at 30 min, with no obvious differences among the three groups, indicating that microneedle injection can act quickly in vivo, just like syringe injection, and the introduction of TPS did not change the

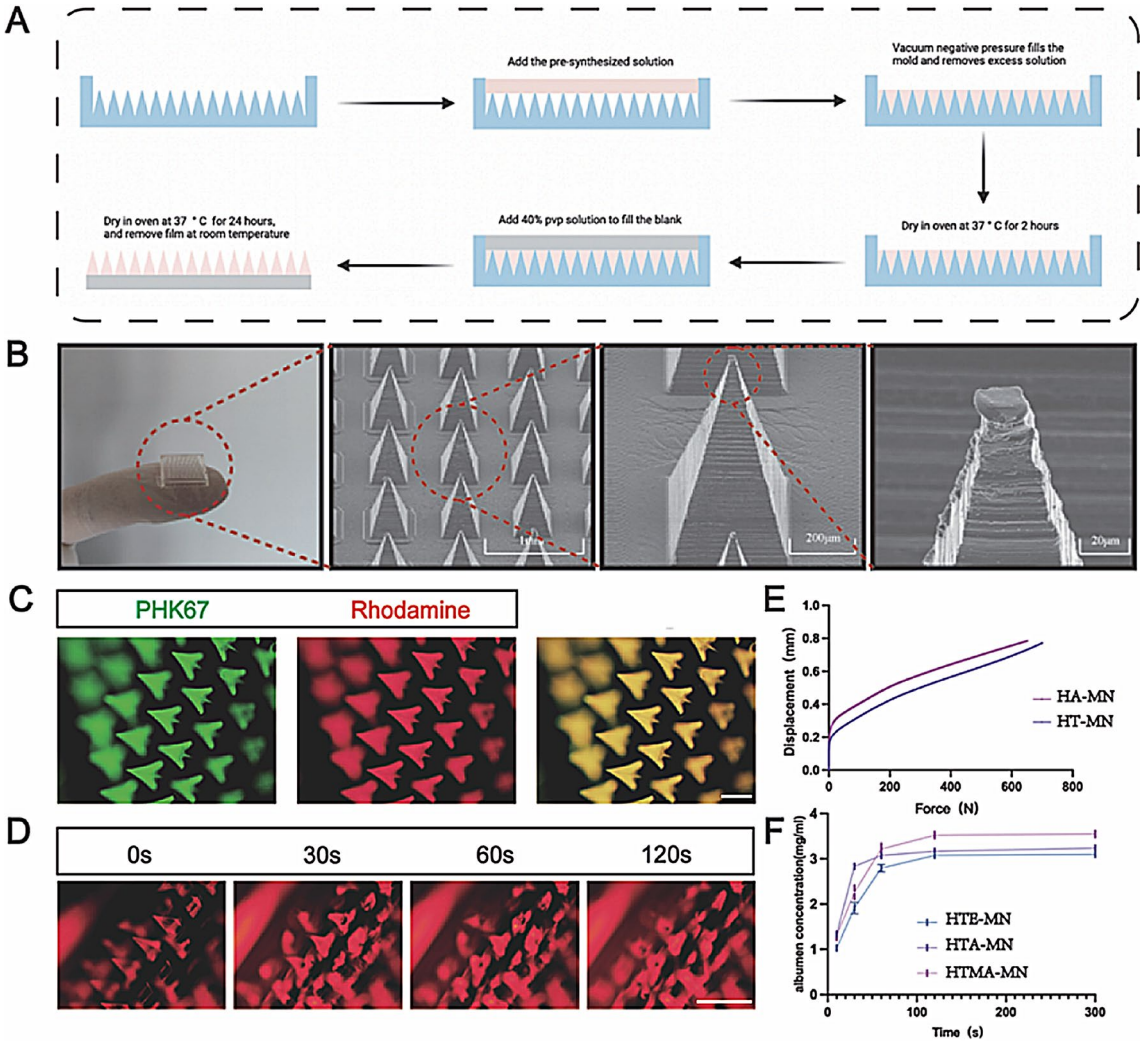

Fig. 5 Preparation and characterization of separable microneedle patches. (**A**) Schematic diagram of the preparation of microneedles using the microneedle mold method. (**B**) Scanning electron microscope (SEM) images of microneedles. (**C**) Representative fluorescence images of microneedles, with microneedle matrix HA-TPS labeled with rhodamine B and DPSC IVs labeled with PKH67. Scale bar: 200 μm. (**D**) Simulated representative images of microneedles in body fluids taken continuously at different times. Scale bar: 200 μm. (**E**) Force displacement curves of HA and HA-TPS microneedles. (**F**) DPSC cell vesicles slow-release curve of microneedles in simulated body fluids

efficiency of HA-MN delivering IVs. Furthermore, the fluorescence completely disappears by day 3, which corresponds to our dosing strategy of once every 3 days.

Certain hair regeneration was observed in all treatment groups. The hair follicles in the HTMI-MN treatment group entered the growth stage on the seventh day and showed the fastest hair regeneration rate. Meanwhile, hair regeneration was observed in both HTE-MN and HTME-MN. Moreover, all the three groups were higher than the minoxidil group (Fig. 6C and G). Physiological analysis of treated skin was performed by hematoxylin and eosin (H&E) staining and immunofluorescence staining. The construction materials of microneedles, including HA, TPS, EVs, IVs and Mag-IVs showed no toxicity (Fig. S3). H&E section staining showed that the hair follicles in the control group remained dormant at day 14, with only a few small hair follicles found, while the activation degree of hair follicles in the treatment group was different (Fig. 6A), and the HTMI-MN group showed more hair follicles and a larger hair follicle diameter (Fig. 6F and H). Ki67 immunohistochemical staining also demonstrated the stimulative effect of MN treatment, with Keratin19 + hair follicle cells observed in all treatment groups, and more hair follicles and Keratin19 + cells were activated in the HTMI-MN group in all treatment groups (Fig. 6A and I). Then, the hair of each group of mice was randomly taken for scanning electron microscopy (SEM) analysis (Fig. 6A) and quantitative analysis showed that the hair width of the DPSC-EVs group was wider and the number of hair scales was more appropriate (Fig. 6E).

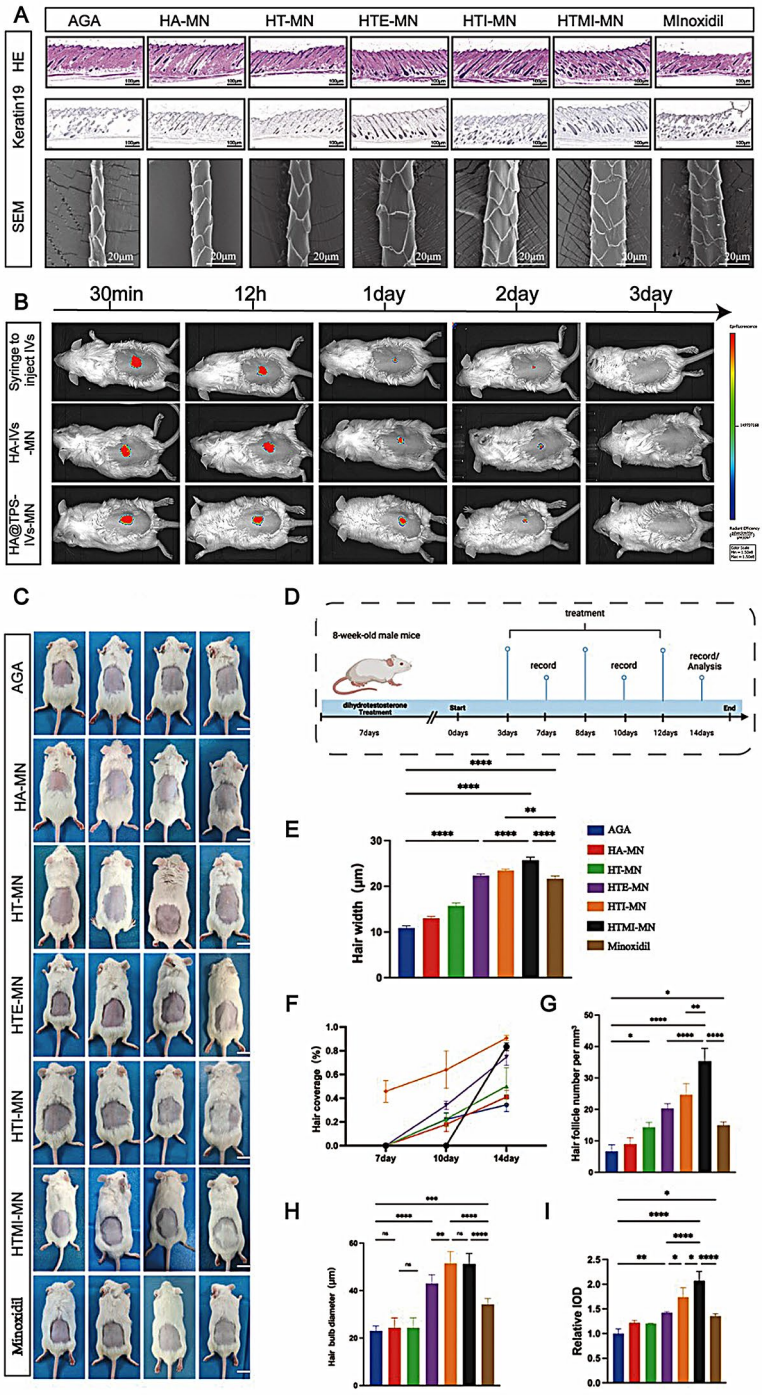

Fig. 6 In vivo evaluation of HTMI-MN for AGA therapy. (**A**) H&E staining images of the alopecia area of mice at 14 days. Keratin19 immunohistochemical staining images of the alopecia area of mice at 14 days. Scanning electron microscopy (SEM) representative images of hair randomly taken from the hair loss area of mice at 14 days. (**B**) DiR labeled IVs was injected directly or encrusted in the tip of HA-MN and HT-MN into the back of mice for in vivo imaging of the hair loss area on the back of mice for 7 days. (**C**) Representative images of mice treated with HI-MN, HT-MN, HTE-MN, HTME-MN, HTMI-MN, and Minoxidil, respectively, Scale bar = 1 cm. (**D**) Schematic diagram of DPSC-EVs treatment for AGA alopecia. (**E**) Quantitative analysis of mouse hair width by SEM in Fig. 6A. (**F**) Quantitative analysis of the coverage area of new hair in Fig. 6C. (**G**) Quantitative analysis of the number of hair follicles in Figure A. (**H**) Quantitative analysis of hair follicle ball diameter in Figure A. (**I**) Quantitative analysis of Keratin19 immunohistochemical analysis in Fig. 6A. The P-values were calculated using one-way ANOVA, $^{*}p < 0.05$, $^{**}p < 0.01$, $^{***}p < 0.001$, $_{****}p < 0.0001$

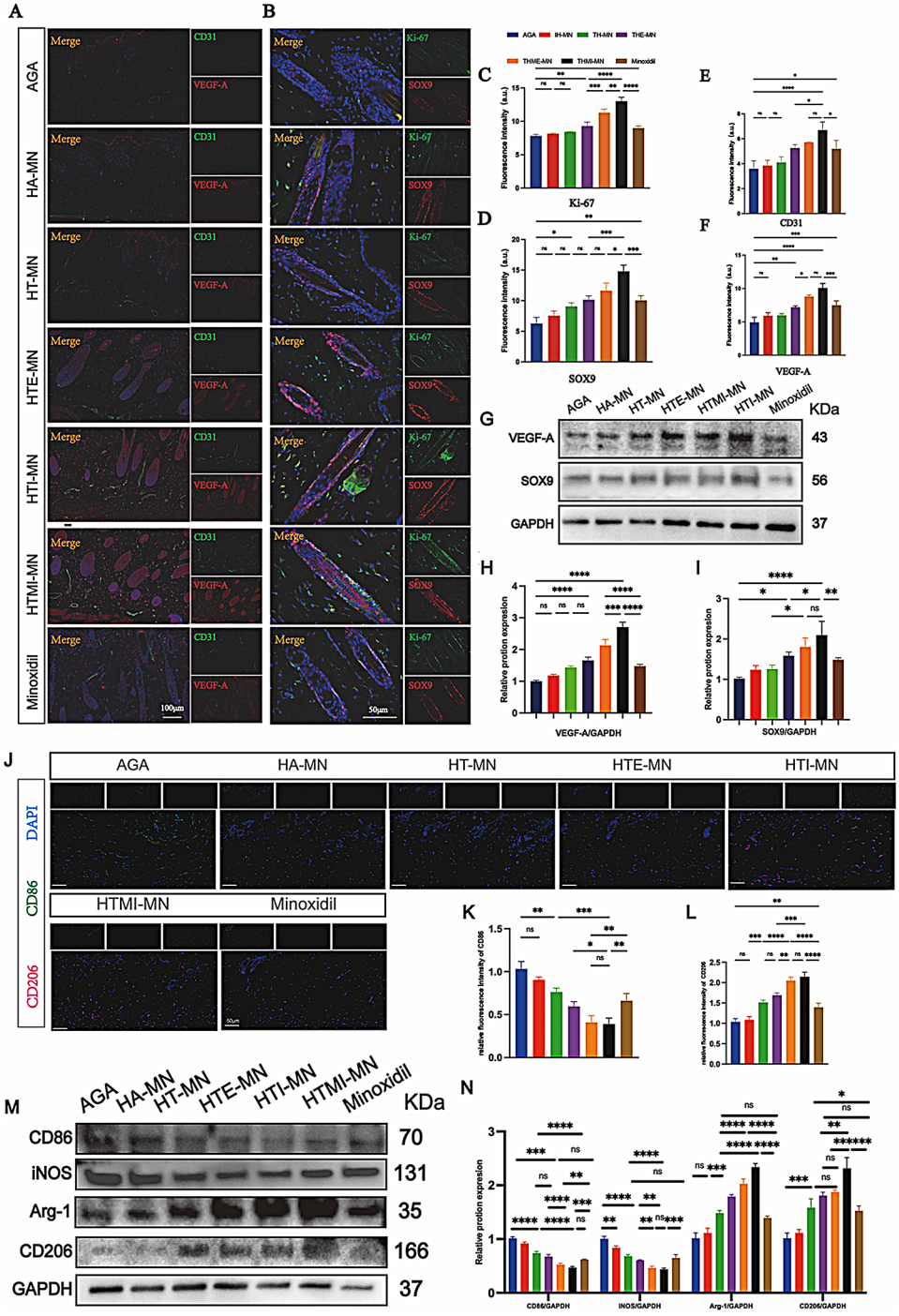

Fig. 7 Immunofluorescence analysis of hair follicle regeneration. (**A**) Representative images of fluorescent staining of CD31 + and VEGF-A + cells in hair follicles. (**B**) Representative images of Ki-67 + and SOX9 + fluorescent staining in hair follicles. Fluorescence quantitative analysis of (**C**) Ki-67 + cells (**D**) SOX9 + cells (**E**) CD31 + cells (**F**) VEGF-A + cells. (**G**) Western Blot was used to detect VEGF-A, SOX9 and GAPDH, and (**H**-**I**) quantitative statistics were performed for gray values. (**J**) Representative images of CD86 + and CD206 + fluorescent staining in skin. Fluorescence quantitative analysis of (**K**) CD86 + cells (**L**) CD206 + cells. (**G**) Western Blot was used to detect CD86, iNOS, Arg-1, CD206 and GAPDH, and (**N**) quantitative statistics were performed for gray values. culture $n = 3$, mean ± SD. ns, nonsignificant ($p > 0.05$), $*p < 0.05$, $**p < 0.01$, $***p < 0.001$, $****p < 0.0001$

In order to more convincingly verify the role of microneedles in vascularization and proliferation promotion, we performed fluorescent staining of CD31, VEGF-A, Ki-67 and SOX9 on mouse skin. As shown in Fig. 7A, due to DHT injury, VEGF-A expression was lower in the modeling group, while DPSC-EVS-loaded microneedles significantly upregulated VEGF-A level, and fluorescent staining of vascular endothelial specific index CD31

showed that the number of blood vessels in the treatment group was higher. Quantitative analysis showed that all treatment groups could improve the level of skin vascularization to a certain extent, and HTMI-MN group had the most obvious effect (Fig. 7E and F). Ki-67 and SOX9 staining also confirmed its role in promoting proliferation. As shown in Fig. 7B, Ki-67 + and SOX9 + cells were found in all treatment groups. Compared with the minoxidil group, MN loaded with DPSC-EVs activated more Ki-67 + and SOX9 + cells, and the effect was most obvious in the HTMI-MN group. To further verify the biological effects of HTMI-MN, the protein expressions of VEGF-A and SOX9 were validated through Western Blot experiments. As shown in Fig. 6G, the protein expression of VEGF-A and SOX9 is similar to the results of immunofluorescence. The proliferation of hair follicle matrix and hair follicle stem cells was accelerated (Fig. 7C and D). These results indicate that HTMI-MN can improve the local microcirculation of mice, accelerate the transformation process of hair follicles from resting period to growth period, promote hair regeneration, and have good hair regeneration effect.

Furthermore, since mesenchymal stem cell EVs have been proven to have excellent anti-inflammatory potential, we further validated the anti-inflammatory capabilities of TPS with different cell vesicles in vivo. Figure 7J shows that the AGA group has high expression of CD86 and low expression of CD206. Although HA-MN can alleviate the effects of AGA to some extent, it is not statistically significant. As we expected, after treatment with HT-MN, the expression of CD86 significantly decreased, while the expression of CD206 increased to some extent, indicating that TPS also possesses certain anti-inflammatory activity in vivo. Moreover, the anti-inflammatory effect of HT-MN is almost similar to that of the standard treatment for androgenetic alopecia, Minoxidil. Furthermore, the expression of CD86 decreased further after treatment with HTE-MN, HTI-MN, and HTMI-MN, while the expression of CD206 significantly increased. Additionally, the effects of HTI-MN and HTMI-MN were similar but higher than those of HTE-MN, indicating that the cell vesicles of DPSC have certain anti-inflammatory effects, with IVs performing better than EVs in terms of anti-inflammatory properties. To further verify, we conducted Western Blot experiments for additional validation. As shown in Fig. 7M, the expression of CD86 and iNOS, which are associated with inflammation and M1 macrophages, was highest after AGA treatment, while the expression of CD206 and Arg-1, which are associated with anti-inflammatory and M2 macrophages, was lowest. The HT-MN treatment group significantly improved this condition and was almost identical to the Minoxidil group. Furthermore, the treatments with HTE-MN, HTI-MN, and HTMI-MN further improved the inflammatory condition, with the anti-inflammatory effect of the HTMI-MN group being the most pronounced, although there was no significant difference in iNOS protein expression and immunofluorescence results compared to the HTI-MN group. In summary, our results show that HTMI-MN has excellent anti-inflammatory effects in vivo, reducing the inflammatory environment caused by androgens, thereby promoting hair regrowth.

Discussion

Acellular regenerative medicine therapies represented by cell vesicles have been widely applied in the treatment of various diseases, such as androgenetic alopecia, vitiligo, hypertrophic scars, or keloids, etc [24–26]. Especially in the field of hair regeneration, the role of EVs has been extensively studied. From a mechanistic perspective, high levels of MMP3 in induced pluripotent stem cell-derived MSCs (iMSCs) derived EVs can activate the Wnt pathway, and precursors of Wnt signaling molecules, such as Wnt3, can promote the proliferation of hair follicle progenitor cells. Additionally, EVs can inhibit growth-downregulating signals (BMP signaling pathway), thereby promoting the transition from the telogen phase to the anagen phase [27, 28].However, the limited yield and high acquisition cost restrict the widespread application of regenerative medicine technologies represented by extracellular vesicles. Our preliminary research found that intracellular vesicles (IVs) derived from the lysis of dental pulp mesenchymal stem cells have a morphology and size similar to EVs, and the content of certain nutritional factors such as BDNF, bFGF, EGF-R, HGF, and PDGF-AA is significantly higher than that of EVs. Moreover, the greatest advantage of IVs is that their yield is approximately 16 times that of EVs. This exponential increase in yield may provide a newer and better option for acellular regenerative medicine therapies [29–31]. IVs is derived from cell lysate, while EVs is derived from cell supernatant, suggesting that IVs can be collected once for the same batch of cells, while EVs can be collected multiple times through repeated cell passage. Nevertheless, IVs can provide a significant increase in efficiency over EVs. However, the mechanism of IVs still needs further study.

Magnetic stimulation of mesenchymal stem cells can further affect the output and bioactivity of EVs. Although the reasons for the increase in EVs production due to magnetic field stimulation still require further research, some studies have already been conducted on their biological functions. For example, magnetic stimulation can enrich more miR-1260a and miR-21-5p in EVs derived from bone marrow mesenchymal stem cells, thereby showing better effects in skin regeneration and bone tissue repair [9, 32]. Since magnetic exosomes are beneficial for tissue repair, we further magnetically produced

DPSC and investigated its yield and function in microenvironmental healing. After magnetic field treatment, we observed that the quantity of IV vesicles made from DPSC grew much more, and the efficacy somewhat improved as well.

AGA is closely related to hair follicle microenvironment damage caused by DHT. Overactivity of DHT produced by 5-alpha-reductase is thought to be the main cause of AGA [33]. DHT leads to oxidative stress damage of hair follicles, resulting in excessive ROS production [6]. Exosomes have been shown to have great potential in regulating oxidative stress and delaying aging [34]. For example, AMSC-EV and HUMSC-EV reduce levels of reactive oxygen species (ROS) and DNA damage, and alleviate UVB-induced inflammation. Mechanistically, proteomics results show that TIMP1 is highly expressed in AMSC-EV and HUMSC-EV. TIMP1 can inhibit Notch1 and its downstream targets Hes1, P16, P21, and P53 [35, 36].Ke Rui et al. found that MSC-EXO weakened OGD/ R-induced neuronal apoptosis and reduced the production of ROS [30]. These results are consistent with our results. Our simulation of DHT injury model shows that ROS content is significantly increased, apoptosis is obvious, and proliferation activity is decreased in DHT-induced group. With the addition of Mag-IVs, apoptosis rate decreased and cell activity increased. This indicates that Mag-IVs has strong ROS scavenging ability.

Research indicates that promoting angiogenesis in areas of hair loss may be beneficial for hair regeneration. However, this important issue has been overlooked in the current development strategies for treating AGA. We investigated the influence of magnetism on the biological function of IVs. Our results show that Mag-IVs, compared to EVs and IVs, can significantly enhance the proliferation, migration, and angiogenic capabilities of HUVEC cells. In vivo experiments also demonstrate an increase in subcutaneous blood vessels after HTMI-MN treatment. This suggests that effectively stimulating angiogenesis does help significantly enhance the effect of AGA therapy.

In addition to DHT attacks, persistent inflammation can also cause AGA [5]. A large number of inflammatory cells gather around the hair follicle, and continue to release inflammatory factors such as TNF-α and IL-6 to gather, attack the hair follicle stem cells and dermal papilla cells, and lead to their inactivation [49]. Exosomal vesicles of mesenchymal stem cells have been found to have excellent immunomodulatory effects. Gareth R Willis et al. found that EXO treatment regulated the expression of inflammation and immune-related genes and promoted M2-like polarization of macrophages [50]. Mechanistically, DPSC-EVs can inhibit osteoclastogenesis and macrophage inflammatory responses through miR-210-3p, thereby suppressing NF-kB1 expression. hUC-EVs induce autophagic flux by inhibiting the activity of mammalian target of rapamycin (mTOR), thereby polarizing M1 macrophages to M2 [37–39]. We have also verified the ability of Mag-IVs to regulate macrophage polarization through in vivo experiments. Western Blot results show that HTMI-MN treatment significantly reduces the expression of CD86 and promotes the expression of CD206, which is also confirmed by immunofluorescence experiments. However, the specific mechanism of action of Mag-IVs remains unclear and requires further exploration.

In summary, cell vesicles can improve the microenvironment of hair follicles and promote hair regeneration by enhancing proliferation, vascularization, resisting ROS, and regulating immunity. To obtain more highly active cell vesicles, we applied magnetic stimulation to DPSC to obtain Mag-IVs. The results showed that Mag-IVs have a similar vesicle structure to EVs and IVs, but with a higher yield. In addition, Mag-IVs can enhance angiogenesis and rescue the apoptosis of hair follicle dermal papilla cells, demonstrating excellent application potential. However, further study is still needed to determine the precise mechanism by which Mag-IVs treat androgenetic alopecia.

Although cell vesicles have strong biological effects, directly injecting cell vesicles to treat skin diseases may lead to issues such as pain, injection depth being too deep or too shallow [15]. Microneedles, as a minimally invasive sustained-release drug delivery system that can penetrate the dermis, have been widely used in the field of dermatology. Improving the structure of the microneedle tips has always been the goal of researchers [40, 41]. For example, microneedle systems loaded with platinum nanobiocatalysts and selenium nanobiocatalysts have been shown to improve the microenvironment by reducing oxidative stress and promoting angiogenesis, thereby regulating hair regeneration [6, 42]. Microneedle systems loaded with ginsenoside Rg3 liposome, hyaluronic acid, and Bletilla striata polysaccharide (BSP) can achieve efficacy comparable to minoxidil under low-frequency treatment, and the quality of regenerated hair is higher [43]. In addition, bioactive substances such as quercetin, mesenchymal stem cell exosomes, and retinoic acid have been used as components of microneedles, primarily activating hair follicle stem cells through the Wnt pathway to treat androgenetic alopecia [44–46]. These studies indicate that microneedle systems have advantages such as painless injection, dermal decomposition, direct activation of hair follicle stem cells, or improvement of the hair follicle microenvironment, making them excellent delivery methods for promoting hair regeneration.

In recent years, the bio-polysaccharide materials of traditional Chinese medicine have been paid more and more attention. Among them, the polysaccharides

from tremella have excellent biocompatibility, biological activity, and immune regulation, which exhibit anti-inflammatory properties that have caught our attention. Mechanistically, the effects of tremella polysaccharides may be related to their ability to block ferroptosis and the accumulation of lipid peroxidation [47]. In addition, tremella polysaccharides can also exert antioxidant effects through free radical degradation [48–50].

In this paper, we proposed the use of tremella polysaccharide/hyaluronic acid microneedles of IVs derived from DPSC treated with magnetic nanoparticles for the treatment of androgenic alopecia. Our results show that HTMI-MN is simple to produce and the cost is significantly lower than that of THE-MN. To prove that each type of material included in the microneedle system can contribute to efficacy, we set up multiple groups to participate in our experiment. Compared to the AGA group, the treatment with HT-MN improved hair recovery to some extent, which can be attributed to the anti-inflammatory effect of TPS. However, the effects of HTE-MN, HTI-MN, and HTMI-MN were significantly stronger than that of HT-MN, indicating that the main therapeutic effect comes from cellular vesicles. Interestingly, the effect of HTMI-MN was stronger than that of HTE-MN and the conventional treatment for androgenetic alopecia, minoxidil. Moreover, microneedles loaded with EVs have already been used in some clinical studies [51, 52]. Therefore, we believe that HTMI-MN has potential clinical translation and application value. However, its therapeutic mechanism is not well understood, and problems such as differences in skin thickness between mice and humans will limit its further application. Therefore, to further explore the specific mechanism of Mag-IVs in the treatment of androgenic alopecia and improve the size and tip morphology of microneedles is an important step in the clinical transformation of microneedles. In addition, the storage and regulatory barriers of HTMN-MN are also important issues affecting clinical applications.

Conclusion

In this work, we designed a TPS-HA/Mag-IVs synthetic microneedle system (HTMI-MN) for the treatment of AGA. The results showed that microneedle treatment was more effective than minoxidil, which is widely used clinically, and had fewer side effects in mouse models. The microneedle system releases Mag-IVs and TPS deep into the dermis, exerting different effects by targeting various pathophysiological processes of AGA. This study demonstrates that microneedles based on TPS and cell vesicles interfere with the progression of AGA in three ways, making it an effective method for treating AGA.

Abbreviations

DPSC	Dental pulp stem cells
IONPs	Iron Oxide Nanoparticles
EVs	Extracellular vesicles
IVs	Intracellular vesicles
Mag-IVs	Magnetic Intracellular vesicles
HA-MN	Microneedles with HA as the base material
HT-MN	Microneedles with HA and TPS as the base material
HTE-MN	A microneedle system containing EVs with HA and TPS as matrix materials
HTI-MN	A microneedle system containing IVs with HA and TPS as matrix materials
HTMI-MN	A microneedle system containing Mag-IVs with HA and TPS as matrix materials
HUVECs	Human Umbilical Vein Endothelial Cells
VEGF	Vascular endothelial growth factor
TPS	Tremella polysaccharide
IL-10	Interleukin-10
IL-1 beta	Interleukin-1 beta
HHDPCs	Human hair papillary cells
TNF-α	Tumor necrosis factor-α
DHT	Dihydrotestosterone
Ki67	Keratin and Intermediate Filament Protein 67
SOX9	SRY-related HMG box gene 9

Supplementary Information

The online version contains supplementary material available at https://doi.org/10.1186/s13287-025-04219-3.

Supplementary Material 1

Acknowledgements

The authors declare that they have not use AI-generated work in this manuscript in this section.

Author contributions

QY, YH designed and wrote the manuscript. LYH contributed to methodology, validation, investigation, and formal analysis. HZ, PPC contributed to revise the content. LY contributed to modify the language. WJN drawn the images. STJY contributed to software. All authors have read and approved the final version of the article.

Funding

This work was supported by the Key Project of Ministry of Science and Technology China (2022YFC2504200); National Natural Science Foundation of China (U22A20314), Chutian Researcher Project (X22020024) and Key R&D Program of Hubei Province of China (YFXM2022000264).

Data availability

All date are available on request. All additional files are included in the manuscript.

Declarations

Ethics approval and consent to participate

About animal testing, study entitled "Tremella polysaccharide microneedles loaded with magnetic dental pulp stem cell intracellular vesicles used for the androgenic alopecia" has been approved by the Experimental Animal Ethics Committee of Wuhan University People's Hospital (date: October 19, 2023, No. 20231003 C) and was conducted in accordance with AVMA guidelines. we had institutional approval for performing experiments using human cells. HUVECs and HHDPCs were obtained from Procell Life Science&Tech (Wuhan, China). Procell Life Science&Tech Company has confirmed that there was initial ethical approval for collection of human cells, and that the donors had signed informed consent.

Consent for publication

Not applicable.

Competing interests

The authors declare that they have no competing interests.

Author details
[1]Center of Regenerative Medicine, Department of Stomatology, Renmin Hospital of Wuhan University, Wuhan 430060, China
[2]Institute of Regenerative and Translational Medicine, Tianyou Hospital of Wuhan University of Science and Technology, Wuhan, Hubei 430064, China
[3]School of Dentistry, The University of Sydney, Sydney, NSW 2006, Australia

Received: 12 November 2024 / Accepted: 11 February 2025
Published online: 31 March 2025

References

1. Žnidarič M, Žurga M Ž, and, Maver U. Design of in Vitro Hair follicles for different applications in the treatment of Alopecia-A Review. Biomedicines. 2021; 9(4).
2. Griggs J, Burroway B, Tosti A. Pediatric androgenetic alopecia: a review. J Am Acad Dermatol. 2021;85(5):1267–73.
3. Yang Y, et al. Curcumin-zinc framework encapsulated microneedle patch for promoting hair growth. Theranostics. 2023;13(11):3675–88.
4. Zhang Z, et al. A combination therapy for androgenic alopecia based on quercetin and zinc/copper dual-doped mesoporous silica nanocomposite microneedle patch. Bioact Mater. 2023;24:81–95.
5. Deng Z, et al. Androgen receptor-mediated Paracrine Signaling induces regression of blood vessels in the dermal papilla in Androgenetic Alopecia. J Invest Dermatol. 2022;142(8):2088–e20999.
6. Yuan A, et al. Ceria Nanozyme-Integrated Microneedles reshape the Perifollicular Microenvironment for Androgenetic Alopecia Treatment. ACS Nano. 2021;15(8):13759–69.
7. Xiong J, et al. Bioinspired engineering ADSC nanovesicles thermosensitive hydrogel enhance autophagy of dermal papilla cells for androgenetic alopecia treatment. Bioact Mater. 2024;36:112–25.
8. Zeng J, et al. M2 macrophage-derived exosome-encapsulated microneedles with mild photothermal therapy for accelerated diabetic wound healing. Mater Today Bio. 2023;20:100649.
9. Wu D, et al. Bone mesenchymal stem cells stimulation by magnetic nanoparticles and a static magnetic field: release of exosomal miR-1260a improves osteogenesis and angiogenesis. J Nanobiotechnol. 2021;19(1):209.
10. He Y, et al. Enhanced osteogenic differentiation of human bone-derived mesenchymal stem cells in 3-dimensional printed porous titanium scaffolds by static magnetic field through up-regulating Smad4. Faseb j. 2019;33(5):6069–81.
11. Kim HY, et al. Mesenchymal stem cell-derived magnetic extracellular nanovesicles for targeting and treatment of ischemic stroke. Biomaterials. 2020;243:119942.
12. Duan X, et al. A new subtype of artificial cell-derived vesicles from dental pulp stem cells with the bioequivalence and higher acquisition efficiency compared to extracellular vesicles. J Extracell Vesicles. 2024;13(7):e12473.
13. Wang R, et al. PROTAC degraders of androgen receptor-integrated dissolving microneedles for Androgenetic Alopecia and Recrudescence Treatment via Single Topical Administration. Small Methods. 2023;7(1):e2201293.
14. Jha AK, Vinay K. Androgenetic alopecia and microneedling: every needling is not microneedling. J Am Acad Dermatol. 2019;81(2):e43–4.
15. Lin S, et al. Strategy for hypertrophic scar therapy: improved delivery of triamcinolone acetonide using mechanically robust tip-concentrated dissolving microneedle array. J Control Release. 2019;306:69–82.
16. Fertig RM, et al. Microneedling for the treatment of hair loss? J Eur Acad Dermatol Venereol. 2018;32(4):564–9.
17. Kim MJ, et al. Minoxidil-loaded hyaluronic acid dissolving microneedles to alleviate hair loss in an alopecia animal model. Acta Biomater. 2022;143:189–202.
18. Zhou H, et al. Metal-organic framework materials promote neural differentiation of dental pulp stem cells in spinal cord injury. J Nanobiotechnol. 2023;21(1):316.
19. Abeysinghe HC, et al. Pre-differentiation of human neural stem cells into GABAergic neurons prior to transplant results in greater repopulation of the damaged brain and accelerates functional recovery after transient ischemic stroke. Stem Cell Res Ther. 2015;6:186.
20. Wu D, et al. Exosomes Derived from Bone mesenchymal stem cells with the Stimulation of Fe(3)O(4) nanoparticles and static magnetic field enhance Wound Healing through upregulated miR-21-5p. Int J Nanomed. 2020;15:7979–93.
21. Yuan A, et al. Conditioned media-integrated microneedles for hair regeneration through perifollicular angiogenesis. J Control Release. 2022;350:204–14.
22. Gu C et al. Local release of copper manganese oxide using HA Microneedle for improving the efficacy of drug-resistant wound inflammation. Small. 2024: e2406377.
23. Odinotski S, et al. A conductive hydrogel-based Microneedle platform for real-time pH measurement in live animals. Small. 2022;18(45):e2200201.
24. Jafarzadeh A, et al. Regenerative medicine in the treatment of specific dermatologic disorders: a systematic review of randomized controlled clinical trials. Stem Cell Res Ther. 2024;15(1):176.
25. Jafarzadeh A, PourMohammad A, Goodarzi A. A systematic review of the efficacy, safety and satisfaction of regenerative medicine treatments, including platelet-rich plasma, stromal vascular fraction and stem cell-conditioned medium for hypertrophic scars and keloids. Int Wound J. 2024;21(4):e14557.
26. Jafarzadeh A, Mohammad AP, Goodarzi A. A systematic review of Case Series and clinical trials investigating Regenerative Medicine for the Treatment of Vitiligo. J Cosmet Dermatol. 2024.
27. Chen Y, et al. Sustained release of dermal papilla-derived extracellular vesicles from injectable microgel promotes hair growth. Theranostics. 2020;10(3):1454–78.
28. Oh HG, et al. Improvement of androgenic alopecia by extracellular vesicles secreted from hyaluronic acid-stimulated induced mesenchymal stem cells. Stem Cell Res Ther. 2024;15(1):287.
29. Dong X, et al. Exosome-mediated delivery of an anti-angiogenic peptide inhibits pathological retinal angiogenesis. Theranostics. 2021;11(11):5107–26.
30. Peng H, et al. Intranasal Administration of Self-oriented Nanocarriers based on therapeutic exosomes for synergistic treatment of Parkinson's Disease. ACS Nano. 2022;16(1):869–84.
31. Riazifar M, et al. Stem cell-derived exosomes as Nanotherapeutics for Autoimmune and Neurodegenerative disorders. ACS Nano. 2019;13(6):6670–88.
32. Wu XD, et al. Exosomes derived from magnetically actuated bone mesenchymal stem cells promote tendon-bone healing through the miR-21-5p/SMAD7 pathway. Mater Today Bio. 2022;15:100319.
33. Kang JI, et al. Hair-loss preventing effect of Grateloupia Elliptica. Biomol Ther (Seoul). 2012;20(1):118–24.
34. Bai L et al. Materiobiomodulated ROS Therapy for De Novo Hair Growth. Adv Mater. 2024: e2311459.
35. Zhang H, et al. Human adipose and umbilical cord mesenchymal stem cell-derived extracellular vesicles mitigate photoaging via TIMP1/Notch1. Signal Transduct Target Ther. 2024;9(1):294.
36. Abdal Dayem A, et al. Engineering extracellular vesicles for ROS scavenging and tissue regeneration. Nano Converg. 2024;11(1):24.
37. Tian J, et al. Small extracellular vesicles derived from hypoxic preconditioned dental pulp stem cells ameliorate inflammatory osteolysis by modulating macrophage polarization and osteoclastogenesis. Bioact Mater. 2023;22:326–42.
38. Su Y, et al. hUC-EVs-ATO reduce the severity of acute GVHD by resetting inflammatory macrophages toward the M2 phenotype. J Hematol Oncol. 2022;15(1):99.
39. Ding JY, et al. Mesenchymal stem cell-derived extracellular vesicles in skin wound healing: roles, opportunities and challenges. Mil Med Res. 2023;10(1):36.
40. Lyu S, et al. Going below and beyond the surface: Microneedle structure, materials, drugs, fabrication, and applications for wound healing and tissue regeneration. Bioact Mater. 2023;27:303–26.
41. Ma G, Wu C. Microneedle, bio-microneedle and bio-inspired microneedle: a review. J Control Release. 2017;251:11–23.
42. Hu W et al. Platinum nanozyme-loaded dissolving microneedles scavenge ROS and promote lineage progression for Androgenetic Alopecia Treatment. Small Methods. 2024: e2401176.
43. Yang Q, et al. Dissolvable microneedles loaded ginsenoside Rg3 liposome: a transdermal delivery approach for alopecia treatment. Regen Biomater. 2024;11:rbae086.
44. Wu X, et al. Hybrid hair follicle stem cell extracellular vesicles co-delivering finasteride and gold nanoparticles for androgenetic alopecia treatment. J Control Release. 2024;373:652–66.
45. Salhab O, Khayat L, Alaaeddine N. Stem cell secretome as a mechanism for restoring hair loss due to stress, particularly Alopecia Areata: narrative review. J Biomed Sci. 2022;29(1):77.

46. Wen L, et al. Retinoic acid drives hair follicle stem cell activation via Wnt/β-catenin signalling in androgenetic alopecia. J Eur Acad Dermatol Venereol. 2025;39(1):189–201.
47. Peng G, et al. Tremella aurantialba polysaccharides alleviate ulcerative colitis in mice by improving intestinal barrier via modulating gut microbiota and inhibiting ferroptosis. Int J Biol Macromol. 2024;281(Pt 4):135835.
48. Wang X, et al. Treatment of ulcerative colitis via the in situ restoration of local immune and microbial homeostasis by oral administration of Tremella polysaccharide drug-carrying hydrogel. Int J Biol Macromol. 2024;285:138223.
49. Zhao X, et al. The comparison of immune-enhancing activity of sulfated polysaccharidses from Tremella and Condonpsis pilosula. Carbohydr Polym. 2013;98(1):438–43.
50. Zhang Z, et al. Free-radical degradation by Fe2+/Vc/H2O2 and antioxidant activity of polysaccharide from Tremella Fuciformis. Carbohydr Polym. 2014;112:578–82.
51. Park GH, et al. Efficacy of combined treatment with human adipose tissue stem cell-derived exosome-containing solution and microneedling for facial skin aging: a 12-week prospective, randomized, split-face study. J Cosmet Dermatol. 2023;22(12):3418–26.
52. Lagrange S, et al. Comparison of microneedling and full surface erbium laser dermabrasion for autologous cell suspension grafting in nonsegmental vitiligo: a randomized controlled trial. Br J Dermatol. 2019;180(6):1539–40.

Publisher's note